Septins promote stress fiber–mediated maturation of focal adhesions and renal epithelial motility

Lee Dolat,[1] John L. Hunyara,[1] Jonathan R. Bowen,[1] Eva Pauline Karasmanis,[1] Maha Elgawly,[1] Vitold E. Galkin,[2] and Elias T. Spiliotis[1]

[1]Department of Biology, Drexel University, Philadelphia, PA 19104
[2]Department of Physiological Sciences, Eastern Virginia Medical School, Norfolk, VA 23507

Organogenesis and tumor metastasis involve the transformation of epithelia to highly motile mesenchymal-like cells. Septins are filamentous G proteins, which are overexpressed in metastatic carcinomas, but their functions in epithelial motility are unknown. Here, we show that a novel network of septin filaments underlies the organization of the transverse arc and radial (dorsal) stress fibers at the leading lamella of migrating renal epithelia. Surprisingly, septin depletion resulted in smaller and more transient and peripheral focal adhesions. This phenotype was accompanied by a highly disorganized lamellar actin network and rescued by the actin bundling protein α-actinin-1. We show that preassembled actin filaments are cross-linked directly by Septin 9 (SEPT9), whose expression is increased after induction of renal epithelial motility with the hepatocyte growth factor. Significantly, SEPT9 overexpression enhanced renal cell migration in 2D and 3D matrices, whereas SEPT9 knockdown decreased migration. These results suggest that septins promote epithelial motility by reinforcing the cross-linking of lamellar stress fibers and the stability of nascent focal adhesions.

Introduction

Embryonic patterning and organogenesis depend on the morphogenetic movements of epithelial cells, which transition to migratory mesenchymal-like cells (Thiery et al., 2009). In the developing kidney, extensive epithelial movements accompany the formation, branching, and tubulogenesis of the ureteric bud (Dressler, 2002; Zegers et al., 2003), and epithelial-to-mesenchymal transition (EMT) underlies renal fibrosis and the metastasis of renal cell carcinomas (RCCs; Liu, 2010; De Craene and Berx, 2013). EMT is characterized by disruption of cell–cell adhesions, cell scattering, and the enhancement of invasive cell motility with a front–rear polarity (Guarino et al., 2007; Lim and Thiery, 2012).

Mesenchymal motility is driven by the actomyosin cytoskeleton and involves adhesion to the ECM and its degradation (Friedl and Wolf, 2010; Bravo-Cordero et al., 2012). Nascent adhesions are stabilized and grow to focal adhesions (FAs) under the tension exerted by a network of actin stress fibers (Schwartz, 2010; Geiger and Yamada, 2011). At the leading lamellae of migrating cells, forces are transduced to adhesions by the radial (dorsal) stress fibers (RSFs), which extend dorsally from FAs and connect with the transverse arc (TA), a contractile network of curved actin filaments (Gardel et al., 2010; Parsons et al., 2010; Burridge and Wittchen, 2013). Actin nucleating and cross-linking proteins and myosin II, whose activity is regulated by the phosphorylation of its regulatory light chain (RLC), mediate the assembly, organization, and contraction of actin stress fibers (Parsons et al., 2010; Burridge and Wittchen, 2013). Actomyosin organization and contractility are regulated by the small GTPases of the Ras superfamily, which affect cell motility (Raftopoulou and Hall, 2004; Parri and Chiarugi, 2010).

Septins are evolutionarily and structurally related to the Ras GTPases (Leipe et al., 2002), but unlike the monomeric small GTPases, septins form filamentous polymers that consist of nonpolar hetero-octameric complexes (Weirich et al., 2008; Mostowy and Cossart, 2012). Septins interact with the actomyosin cytoskeleton (Kinoshita et al., 2002; Joo et al., 2007; Mavrakis et al., 2014) and are abnormally overexpressed in RCCs, but their precise function in stress fiber organization and mesenchymal-like

Correspondence to Elias T. Spiliotis: ets33@drexel.edu

Abbreviations used in this paper: EMT, epithelial-to-mesenchymal transition; FA, focal adhesion; FCF, forchlorfenuron; HGF, hepatocyte growth factor; RCC, renal cell carcinoma; RLC, regulatory light chain; RSF, radial stress fiber; SIM, structured illumination microscopy; TA, transverse arc; TIRF, total internal reflection fluorescence.

The Rockefeller University Press $30.00
J. Cell Biol. Vol. 207 No. 2 225–235
www.jcb.org/cgi/doi/10.1083/jcb.201405050

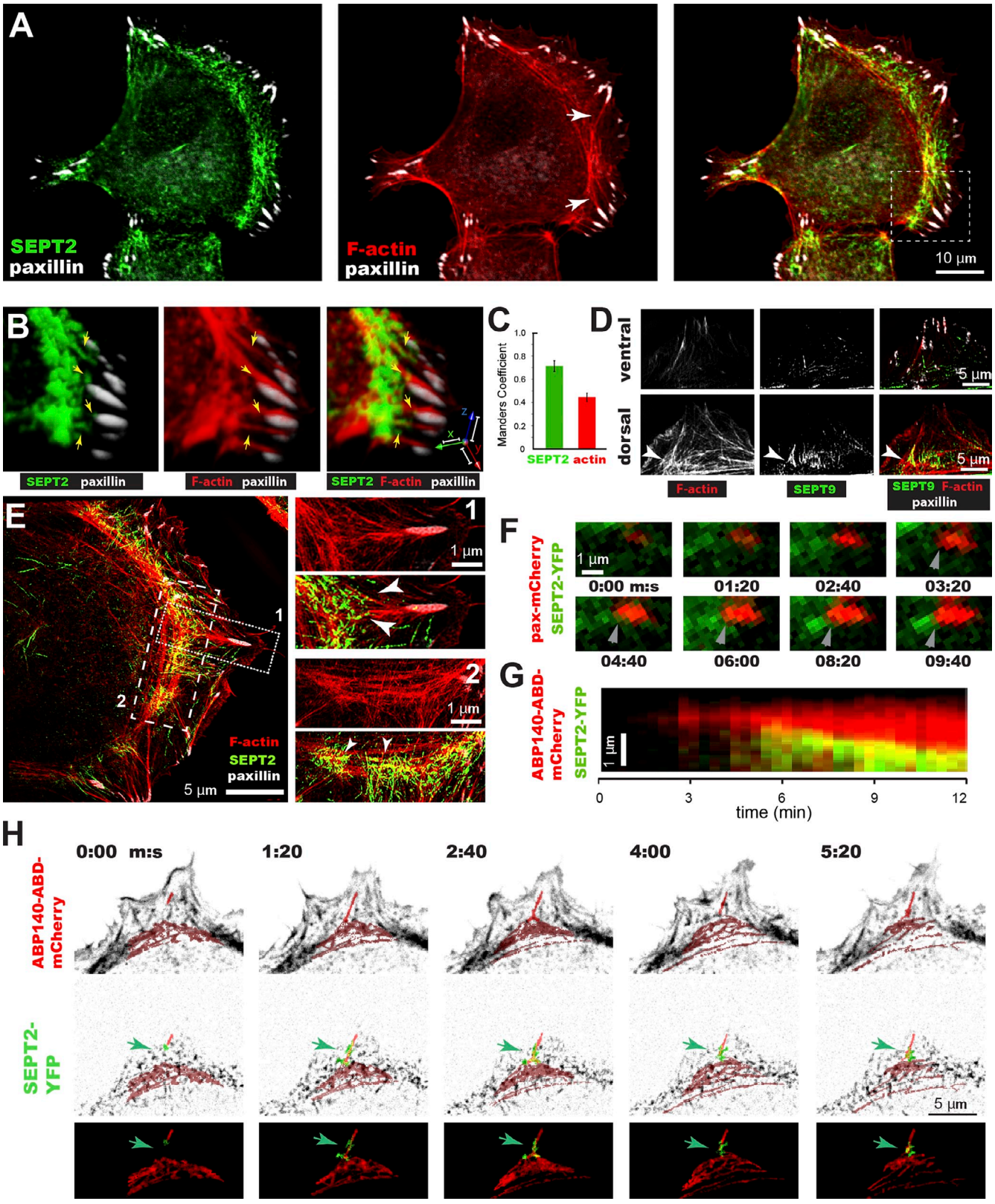

Figure 1. **Septin filaments interface with RSF and TA stress fibers in the leading lamellae of renal epithelia.** (A) Confocal images of SEPT2 (green), actin stress fibers (phalloidin; red), and FAs (paxillin; white) in HGF-treated (16 h) MDCK epithelia. White arrows point to RSFs that connect with the TA. (B) 3D rendering of the lamellar region outlined in A. Arrows point to SEPT2 fibers that localize on FA-anchored RSFs. Bars, 1 µm. (C) Quantification of SEPT2 colocalization with F-actin (green) and vice versa (red). Error bars indicate SEM. (D) SIM images show ventral and dorsal optical sections from the lamellar region of an HGF-treated MDCK cell. The arrowhead points to SEPT9 localization on the dorsal segment of an RSF that connects with the TA. (E) SIM images show an HGF-treated MDCK cell stained for F-actin (phalloidin; red), SEPT2 (green), and paxillin (white). FA-anchored RSF (1) and TA filaments (2) are shown in higher magnification. Arrowheads point to SEPT2 localization on and between actin filaments. (F) Still frames show FA formation

motility is unknown. Here, we show that in the leading edge of motile renal epithelia, a novel network of septin filaments promotes cell motility by reinforcing the organization of the lamellar stress fiber network and the stability of nascent FAs.

Results and discussion

A network of septin filaments interfaces with RSF and TA stress fibers in the leading lamella of renal epithelia

To examine septin functions in the motility of renal epithelia, we used the MDCK model of partial EMT, which allows the study of cell migration in 2D and 3D matrices after stimulation with the hepatocyte growth factor (HGF; Zegers et al., 2003). Treatment of MDCKs with HGF disrupted cell–cell adhesions and induced scattering and development of front–rear cell polarity, as shown previously (de Rooij et al., 2005). Resembling the stress fiber organization of migratory cells, the lamellae of fan-shaped MDCK cells contained RSFs that extended dorsally from FAs and connected with TA filaments (Fig. 1 A, arrows). Staining for endogenous Septin 2 (SEPT2), SEPT6, SEPT7, and SEPT9 revealed an extensive network of septin filaments that localized at the interface of TA filaments and RSFs (Fig. 1 A and Fig. S1, A–C). Colocalization and coimmunoprecipitation of SEPT2, SEPT6, SEPT7, and SEPT9 (Fig. S1, D–G) indicated that these septin filaments consist of SEPT2/6/7/9 complexes, which are the basic structural units of mammalian septin filaments (Kim et al., 2011; Sellin et al., 2011). Thus, we used SEPT2 as a marker for the lamellar network of septin fibers, and SEPT2 and SEPT9 shRNAs were interchangeably applied to perturb the localization and function of septins; knockdown of SEPT2 or SEPT9 affected the expression and localization of both of these septins as well as SEPT6 and SEPT7 (Fig. S2, A and B), as reported previously (Kim et al., 2011).

To determine the precise localization of septins with respect to the lamellar network of stress fibers and FAs, we used confocal microscopy in combination with 3D image reconstructions and super-resolution structured illumination microscopy (SIM). Septins localized mainly on and between the curved actin bundles of the TA network and on a subset of RSFs (Fig. 1, B–E; and Video 1). Septins were present on the dorsal ends of 80 ± 2% RSFs (n = 72; 12 cells) that connected with the TA (Fig. 1, B and D). On the quartile end of these RSFs, 1.9 ± 0.16 µm away from FAs (n = 58; 12 cells), septins interdigitated with actin filaments as they flared from their FA-anchored bundle toward the TA (Fig. 1 E, panel 1). Time-lapse microscopy showed that septins are recruited to the distal ends of RSFs after the assembly of nascent FAs (Fig. 1, F and G). In live cells, septins persisted on RSFs during their interactions with the TA, spanning segments of both RSF and TA stress fibers (Fig. 1 H). Collectively, these data indicate that septins localize at the interface of the contractile TA and RSFs, and thus may be part of the actomyosin machinery that drives the growth and turnover of nascent FAs in motile renal epithelia.

Septins are required for the stabilization of nascent FAs and the organization of the lamellar stress fiber network

To test whether septins affect the formation and dynamics of FAs, HGF-treated MDCK epithelia were depleted of SEPT2 or SEPT9. Septin knockdown with two different SEPT2 shRNAs and a SEPT9 shRNA increased the number of FAs, which were smaller and localized closer to the cell edge compared with control cells (Fig. 2, A–D). Time-lapse imaging of paxillin-GFP showed that septin knockdown reduces the lifetime of nascent FAs (Fig. 2 E), which fail to grow significantly in size and do not move closer to the cell body (Video 2). Analysis of the kinetics of paxillin-GFP fluorescence revealed no differences in the rates of FA assembly and disassembly (Fig. 2 F), but septin depletion abolished the stabilization phase of the FA life cycle (Fig. 2 G). Consistent with the lack of FA stabilization, which is characterized by dephosphorylation of paxillin's Tyr118 (Zaidel-Bar et al., 2007), septin depletion increased the levels of pTyr118-paxillin relative to total paxillin in MDCK and 786-O RCC cells (Fig. 2, H and I).

Maturation of nascent FAs is mediated by stress fibers, which exert mechanical forces and provide a template for the growth of cell–ECM adhesions (Vicente-Manzanares et al., 2009; Gardel et al., 2010; Burridge and Wittchen, 2013). Although myosin-mediated tension is thought to be the main trigger of FA maturation, recent work shows that myosin II–dependent tension is necessary but not sufficient for FA maturation, which requires actin-binding proteins that mediate the formation and maintenance of the lamellar actin network (Choi et al., 2008; Oakes et al., 2012; Roca-Cusachs et al., 2013; Stricker et al., 2013).

Next, we examined the organization and dynamics of the lamellar actin network in septin-depleted cells. Strikingly, the lamellar actin meshwork was thin and devoid of an organized TA (Fig. 2 J). F-actin was significantly reduced in the lamellar regions of the cell (5–10 µm from the cell edge; Fig. 2 K), and the length and density of RSFs decreased by ∼50% (Fig. 2, L and M). In live SEPT2-depleted cells, RSFs were short-lived, dissipating quickly after their formation, whereas in control cells the actin fluorescence of RSFs persisted and increased over time (Fig. 2 N and Video 3). Taken together with the localization of septins to the TA and distal ends of RSFs, these data suggest that septins are required for the stabilization and maturation of nascent FAs by maintaining the organization and possibly the contractility of the lamellar stress fiber network.

(paxillin-mCherry; red) and subsequent recruitment of SEPT2-YFP (green). Arrows point to septin accumulation at the distal end of a nascent focal adhesion. (G) TIRF microscopy kymograph shows recruitment of SEPT2-YFP (green) to a nascent RSF (ABP140-ABD-mCherry, red). (H) Inverted monochrome images show frames from spinning disk confocal time-lapse microscopy of HGF-treated MDCK cells expressing ABP140-ABD-mCherry and SEPT2-YFP. A subset of TA filaments and an RSF were pseudo-colored red and superimposed onto the inverted monochrome image of the SEPT2-YFP channel. SEPT2-YFP elements recruited to the junction of the RSF with the TA were pseudo-colored green. The overlay image shows the pseudocolored stress fibers and SEPT2 outlined in the inverted monochrome frames. The arrow points to the RSF end and its junction point with the TA.

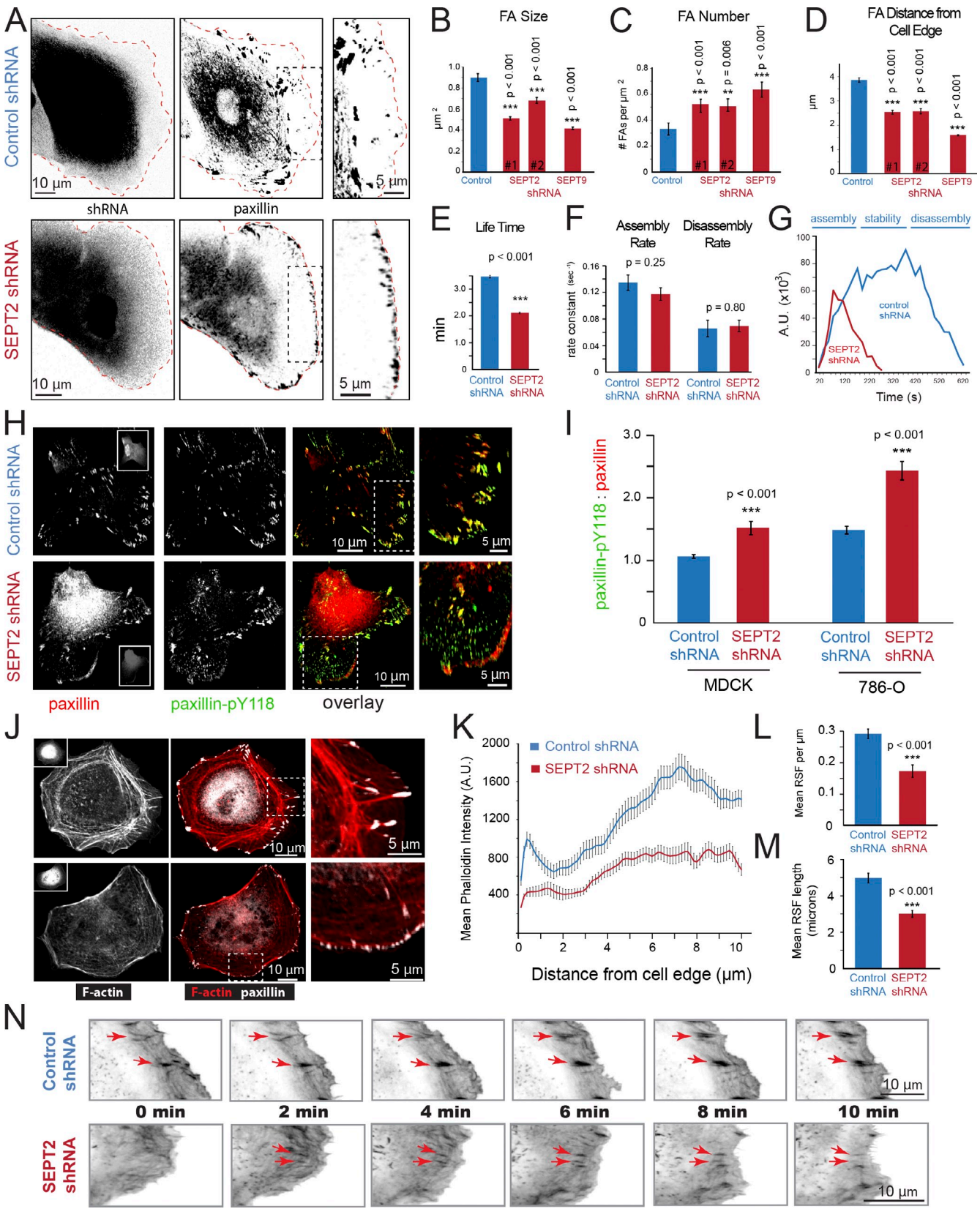

Figure 2. **Septins regulate the organization of the lamellar actin network and are required for the stabilization of nascent FAs.** (A) Confocal images of MDCK cells, which were transfected with mCherry-expressing plasmids that encode for control or SEPT2 shRNAs and stained for paxillin after treatment with HGF. The red broken line highlights the cell edge. Panels on the right show enlarged views of the black boxed region. (B and C) Graphs show FA size and number from MDCK cells (n = 20) treated with control, SEPT2, and SEPT9 shRNAs. (D) Graph shows FA distance from the cell edge of MDCK cells (n = 10) treated with control (n = 903 FAs), SEPT2 #1 (n = 749 FAs), SEPT2 #2 (n = 512 FAs), and SEPT9 shRNAs (n = 840 FAs). (E) The graph shows FA lifetime in three different MDCK cells treated with control (n = 6,066 FAs) and SEPT2 shRNAs (n = 10,528 FAs). (F) The graph shows the rates of FA

Septins function as actin cross-linking proteins in FA maturation

Because SEPT2 binds myosin II directly and this interaction is posited to facilitate the activation of the myosin RLC (Joo et al., 2007), we sought to determine whether septins affect FA maturation through their role in the organization of the lamellar actin network or by a possible involvement in myosin-mediated tension. To distinguish between these possibilities, we first tested whether septins affect the levels of activated myosin RLC on the contractile TA, and second whether the actin bundling protein α-actinin-1 or the constitutively active di-phosphomimetic myosin RLC-DD can rescue septin loss of function. Analysis of the fluorescence intensity ratio of the phosphorylated pSer19 myosin RLC to total myosin IIA showed no difference between control and SEPT2-depleted cells (Fig. S3, A and B). In agreement, RLC-DD did not rescue FA size and number in SEPT2-depleted cells (Fig. 3, A–C). In contrast, α-actinin-1 restored the number and size of FAs to near control levels (Fig. 3, A–C). This effect of α-actinin-1 was also accompanied by a rescue of the lamellar actin network in septin-depleted cells, which now contained a network of TA filaments and RSFs (Fig. 3 D). Notably, α-actinin-1-ΔABD, which lacks its actin-binding domain, did not rescue FAs (Fig. 3, B and C), whereas the actin-binding motor-dead myosin II-N93K did (Fig. S3, C–E). Thus, loss of septin function in FA maturation is specifically rescued by the actin-binding and cross-linking properties of α-actinin-1 and myosin IIA heavy chain.

Previous studies have reported that septin complexes comprising of SEPT2, SEPT6, and SEPT7 do not bind actin filaments directly (Kinoshita et al., 2002), but new work shows that co-polymerization of actin with SEPT2/6/7 results in circular actin filaments (Mavrakis et al., 2014). Because septins interact with preassembled RSFs and TA filaments in the lamellar regions of motile MDCK epithelia, we examined whether septins have the ability to cross-link prepolymerized actin filaments using low-speed actin sedimentation assays and negative stain EM. We found that SEPT9 directly cross-links prepolymerized actin filaments into bundles, whereas SEPT2/6/7 does not (Fig. 3, E–G). These results suggest that septins promote the maturation of nascent FAs by cross-linking the lamellar stress fibers of motile epithelia.

SEPT9 is up-regulated in renal epithelia undergoing EMT and enhances renal cell migration

Given that septins are overexpressed in RCCs and other cancers (Craven et al., 2006; Connolly et al., 2011a; Dolat et al., 2014), we asked whether SEPT9 is up-regulated during renal EMT. Treatment of MDCK cells with HGF increased the levels of SEPT9 relative to actin, whereas actin levels did not change (Fig. 4, A and B). To test if increased SEPT9 expression promotes cell motility, we established stable MDCK cell lines expressing SEPT9-mCherry at low endogenous-like and high levels of expression (Fig. S2, C and D), and cultured these cells in a 3D ECM, which enables the morphogenesis of renal cysts. Treatment of the 3D MDCK cysts with HGF causes tubulogenesis, a process that mimics the collective and invasive migration of metastatic tumors (Debnath and Brugge, 2005). Overexpression of SEPT9 doubled the number of multicellular extensions that protruded from the main cyst, and the extensions were longer and contained more cells (Fig. 4, C and D). In contrast, treatment of cysts with forchlorfenuron (FCF), a septin-targeting compound (Hu et al., 2008), significantly reduced the number of HGF-induced extensions (Fig. 4 E). Moreover, dissociated single MDCK cells migrated slower in 3D and were less elongated and fibroblast-like after SEPT9 depletion (Fig. 4, H and I; and Video 4). To corroborate the effects of SEPT9 overexpression on renal cell motility, we performed a transmigration assay using the 786-O renal carcinoma cells. SEPT9 overexpression increased the migration of 786-O cells along a serum gradient, whereas SEPT9 knockdown decreased migration (Fig. 4, F and G). These results therefore indicate that SEPT9 promotes the mesenchymal-like migration of renal epithelia.

Previous studies have implicated septins in the amoeboid motility of T cells and neuronal migration (Tooley et al., 2009; Shinoda et al., 2010), which are mechanistically different from the stress fiber–driven mode of mesenchymal migration. Septins have been reported to colocalize with stress fibers in fibroblasts (Kinoshita et al., 1997; Schmidt and Nichols, 2004; Kremer et al., 2007), but this interaction has been considered to be indirect (Kinoshita et al., 2002; Joo et al., 2007), and the precise functions of septins in epithelial and mesenchymal motility are unknown (Chacko et al., 2005; Connolly et al., 2011b). Here, we have found that septins are required for the stabilization of nascent FAs. Our results indicate that septins cross-link stress fibers, maintaining the organization of the lamellar actin network, and thereby promoting the transmission of forces from the contractile TA to FAs. This septin function relies on the ability of SEPT9 to cross-link preassembled actin filaments. Thus, septin up-regulation might be part of the EMT program that retools the actin cytoskeleton for a migratory mesenchymal-like phenotype.

(n = 45) assembly and disassembly in cells treated with control and SEPT2 shRNAs. (G) Representative profiles of the kinetics of paxillin-GFP fluorescence in MDCK cells treated with control and SEPT2 shRNAs. (H) Confocal images show 786-O cells stained for total paxillin (red) and phosphorylated pY118-paxillin (green). Insets show GFP expression from plasmids encoding for control and SEPT2 shRNAs. Panels on the right show enlarged views from the boxed regions. (I) Bar graphs show the ratio of the fluorescence intensity of pY118-paxillin to total paxillin in MDCK cells (n = 10) treated with control (n = 740 FAs) and SEPT2 shRNAs (n = 962 FAs), and 786-O cells (n = 10) treated with control (n = 757 FAs) and SEPT2 shRNAs (n = 602 FAs). (J) Confocal images of control and SEPT2-depleted MDCK cells stained for F-actin (phalloidin; red) and paxillin (white). Insets show GFP expression from plasmids encoding for control and SEPT2 shRNAs. Panels on the right show enlarged views of the boxed region. (K) The plot shows line scans of phalloidin fluorescence across the leading edges of MDCK cells (n = 13) treated with control (n = 54 line scans) and SEPT2 shRNAs (n = 56 line scans). Fluorescence quantifications were performed with a custom MATLAB code (supplemental code 1). (L and M) Graphs show the mean number of RSFs per lamellar length (L) and mean length of RSFs (M) in MDCK cells treated with control (n = 43) and SEPT2 shRNAs (n = 72). (N) Inverted monochrome frames show ABP140-ABD-mCherry from total internal reflection fluorescence (TIRF) microscopy of MDCK cells treated with control or SEPT2 shRNAs and HGF. Arrows point to RSFs that persist and grow over time in control cells, and stress fibers that dissipate in SEPT2-depleted cells. Error bars indicate SEM. **, $P < 0.01$; ***, $P < 0.001$.

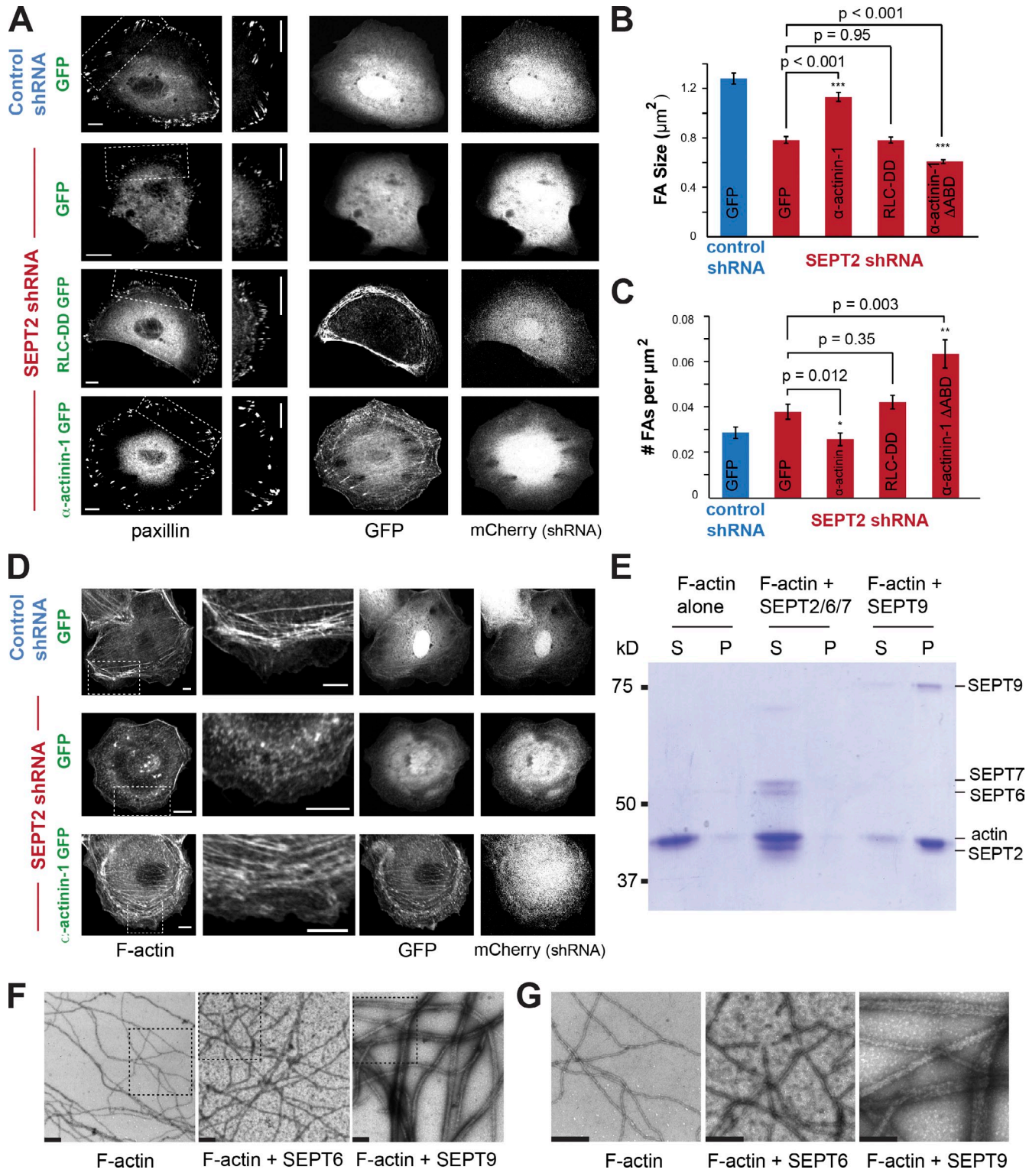

Figure 3. **SEPT9 functions as an actin cross-linking protein in FA maturation.** (A) Confocal images of paxillin-stained MDCK cells transfected with mCherry-expressing plasmids that encode for control or SEPT2 shRNAs, and RLC-DD-GFP, α-actinin-GFP, or GFP vectors. The boxed regions are enlarged in the panels on the immediate right. Bars, 10 µm. (B and C) Graphs show FA size (B) and number per square micrometer (C) in control cells expressing GFP (n = 1,650 FAs; 25 cells), and SEPT2 knockdown cells expressing GFP (n = 1,567 FAs; 24 cells), α-actinin-1-GFP (n = 1,556 FAs; 20 cells), RLC-DD-GFP (n = 1,962 FAs; 18 cells), and α-actinin-1-ΔABD-GFP (n = 1,962 FAs; 20 cells). Error bars indicate SEM. *, P < 0.05; **, P < 0.01; ***, P < 0.001. (D) Confocal images of MDCK cells transfected with mCherry-expressing plasmids encoding for control or SEPT2 shRNAs, and α-actinin-1-GFP or GFP vectors. Cells were stained for F-actin (phalloidin). The boxed regions are enlarged in the panels on the immediate right. Bars, 10 µm. (E) The Coomassie-stained gel shows equal volumes of supernatant (S) and pellet (P) fractions from low-speed sedimentation of prepolymerized actin filaments in the presence of recombinant SEPT2/6/7 and SEPT9. (F and G) Negative stain EM images of actin filaments in the absence and presence of recombinant SEPT6 or SEPT9. Boxed regions (F) are shown at a higher magnification in G. Bars, 0.5 µm.

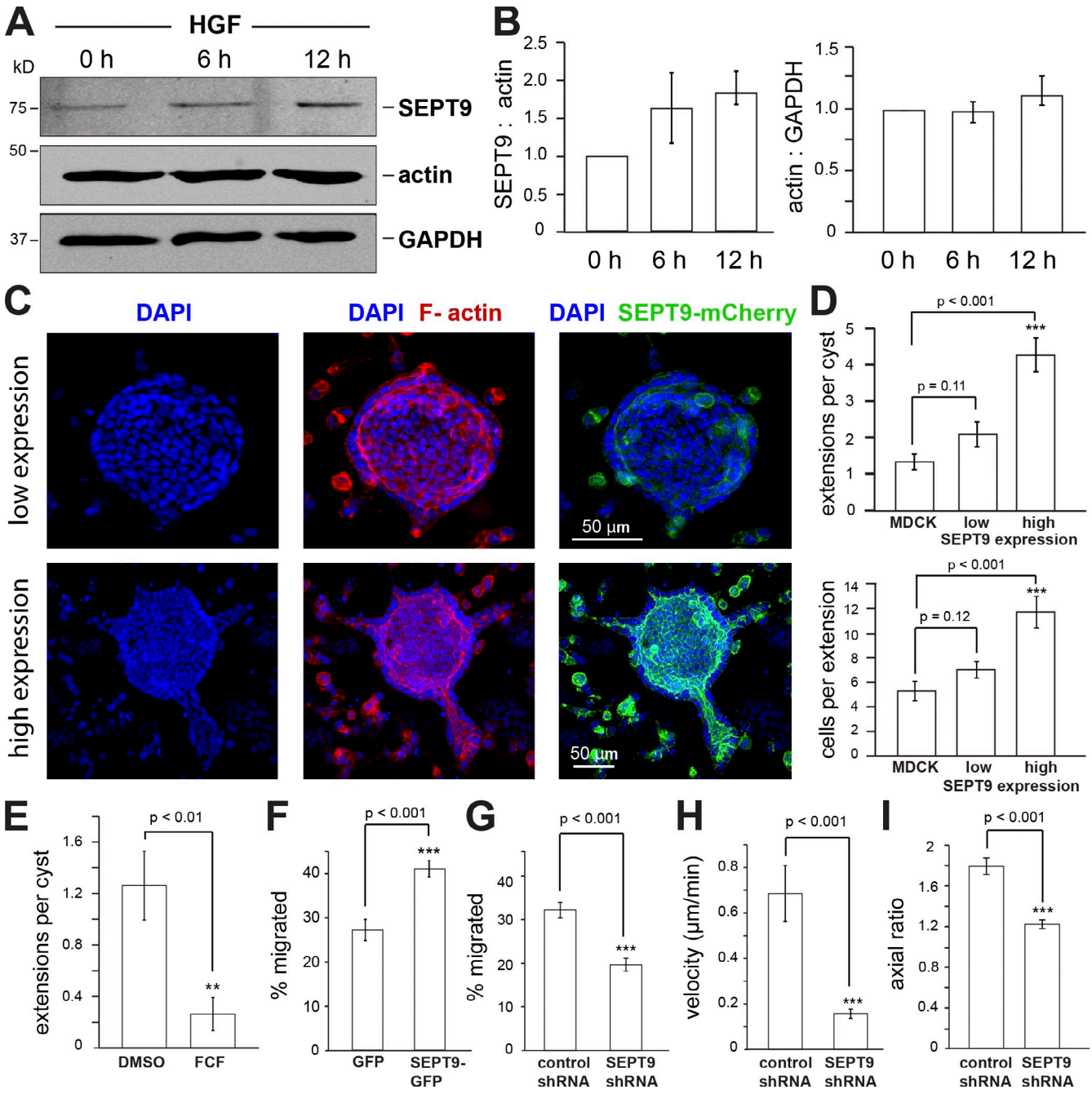

Figure 4. **SEPT9 promotes the motility of renal epithelia during EMT.** (A) Western blot of HGF-treated MDCK cell lysates probed for SEPT9, actin, and GAPDH. (B) Graphs show the median, lowest, and highest (error bars) ratio values of the SEPT9, actin, and GAPDH band intensities from three independent experiments. Values were normalized to the protein band intensity ratios at 0 h of HGF treatment. (C) Maximum intensity projections from 3D confocal microscopy images of HGF-treated renal cysts of stable MDCK cells expressing SEPT9-mCherry (green) at low and high levels of expression. 3D renal cysts were grown in collagen and stained for nuclei (DAPI; blue) and F-actin (phalloidin; red). (D) Graphs show the number of extensions per MDCK cyst (n = 23) and the number of cells per extension from untransfected (n = 18), low-expressing (n = 35), and high-expressing (n = 51) MDCK cysts (n = 15). (E) Mean number of extensions per cyst after treatment with DMSO (n = 23) and FCF (n = 19). (F and G) Graphs show the mean percentage of transmigrated 786-O cells expressing GFP and SEPT9-GFP (F), and control and SEPT9 shRNAs from 20 different areas of a transwell filter. (H and I) Graphs show the mean velocity (H; n = 16) and axial ratio of the long to short axes (I; n = 31) of MDCK cells migrating in a 3D matrix in the presence of HGF after transfection with control or SEPT9 shRNAs. Error bars indicate SEM. **, P < 0.01; ***, P < 0.001.

Materials and methods

Tissue culture and transfections

MDCK II/G cells and the stable MDCK-SEPT2-YFP (N1-YFP, cytomegalovirus [CMV] promoter; Spiliotis et al., 2005), MDCK-paxillin-GFP (C1-EGFP, CMV promoter; Yamada and Nelson, 2007; a gift from J. Nelson, Stanford University, Stanford, CA), MDCK-SEPT9-mCherry (pmCherry-C1, CMV promoter), and MDCK-ABD-ABP140-mCherry (pmCherry-N1, CMV promoter) cell lines were cultured in low-glucose DME with 1 g/liter $NaHCO_3$, 10% FBS (Cell Generation), and 1% PSK (penicillin, streptomycin, and kanamycin) at 5% CO_2. The stable MDCK-SEPT9-mCherry and MDCK-ABP140-mCherry cells were generated by standard selection with G418 sulfate (0.8 mg/ml; Corning), stable transfectants were cloned in 96-well plates by serial dilutions, and levels of expression were analyzed by Western

blotting. The RCC 786-O cell line was purchased from the ATCC and maintained in RPMI with 1 g/liter $NaHCO_3$, 10% FBS, and 1% PSK. Coverslips were acid-washed with 1 M HCl for 4 h at 50°C and coated with 10–20 µg/ml fibronectin (Invitrogen) for 2 h at 37°C or rat tail collagen. Cells were transfected with 1.5 µg of plasmid or cotransfected with 1.5 µg plasmid and 1 µg shRNAs with Lipofectamine 2000 (Invitrogen). Before fixation or live imaging, MDCK cells were stimulated with 20 ng/ml recombinant HGF (Sigma-Aldrich) in DME supplemented with 0.5% FBS for at least 6 h. Live imaging studies were performed in phenol red–free media containing 20 mM Hepes.

To generate polarized cysts, MDCK cells and cells that stably express SEPT9-mCherry at low and high levels were cultured in collagen gels composed of 2 mg/ml type I collagen (Advanced Biomatrix) on transwell filters (0.4 µm pore; BD) for 10 d. Polarized cysts were stimulated with 30 ng/ml HGF for 3 d (Fig. 4, C–E) and with or without 50 µm FCF (Fig. 4 E). To image and quantify single cell migration in 3D (Fig. 4, H and I), MDCK cells were transfected with control or SEPT9-targeting shRNAs for 24 h on tissue culture plates. Cells were dissociated by trypsinization and cultured in 2 mg/ml type I collagen gels on 35-mm glass-bottom dishes (live imaging of MDCK-ABP140-ABD-mCherry; Fig. 4 H) or transwell filters (morphometric analysis of fixed MDCKs; Fig. 4 I) and treated with 40 ng/ml HGF, 16 h before imaging.

Plasmids and shRNAs

Canine SEPT2 was targeted with control (5′-TGAGTTCACACTAATGGTGGTCG-3′), SEPT2 shRNA #1 (5′-CCTTAGACGTCGCATTCATGAAA-3′), and SEPT2 shRNA #2 (5′-GCAACTACAAGCCCGAAGAATAA-3′; Bowen et al., 2011). To target human SEPT2, the SEPT2 shRNA 5′-AAGGTGAATATTGTGCCTGTC-3′ was subcloned into the GFP-expressing pG-SUPER vector. The SEPT9 shRNA construct was made by inserting the SEPT9 shRNA 5′-GACCGGCTGGTGAACGAGAAGTT-3′ into mCherry-expressing pSuper vector. The shRNA constructs against canine and human SEPT9 were made by subcloning the shRNAs 5′-GACCGGCTGGTGAACGAGAAGTT-3′ and 5′-GACCATCGAGATCAAGTCC-3′ into the mCherry-expressing pSuper and GFP-expressing pGFP-V-RS vectors, respectively. ABP140-ABD-mCherry was generated by annealing the primers 5′-ATCCTCCTCCTTGCTGATGCTTCGAACTTCTTGATCAGGTCGGCCACGCCCATGGTGGCG-3′ (forward) and 5′-AATTCGCCACCATGGGCGTGGCCGACCTGATCAAGAAGTCGAGAGCATCAGCAAGGAGG-3′ (reverse), which correspond to the first 17 amino acids (Lifeact) of ABP140, and inserting the sequence into the N1-mCherry vector (Invitrogen) using the NcoI restriction site. SEPT9_mCherry was constructed by PCR amplification of SEPT9_i1 (a gift from C. Montagna, Albert Einstein College of Medicine, Bronx, NY) from pET28a-SEPT9_i1 (Bai et al., 2013) using the primers 5′-CGTAAGCTTGCATGAAGAAGT-3′ and 5′-GTAGTCGACCTACATCTCTGGGGC-3′, and the product was ligated into the HindIII and SalI sites of the pmCherry-C1 vector. Mouse SEPT2 was inserted into N1-YFP (Spiliotis et al., 2005). Avian paxillin was inserted into C1-EGFP (West et al., 2001; the plasmid was a gift from R. Horwitz, University of Virginia, Charlottesville, VA). Mouse myosin IIA-GFP, human α-actinin-1-GFP, and human myosin II RLC-DD-GFP (pEGFP-MRLC1 T18D, S19D) were purchased from Addgene. The actin-binding domain of α-actinin-1 (amino acids 30–253) was deleted from α-actinin-1–GFP (Roca-Cusachs et al., 2013); the plasmid was a gift from P. Roca-Cusachs (University of Barcelona, Barcelona, Spain). The myosin IIA-N93K-GFP mutant was generated by site-directed mutagenesis using the primers 5′-CTCACGTGCCTCAAGGAAGCTTCGGTG-3′ (forward) and 5′-CACCGAAGCTTCCTTGAGGCACGTGAG-3′ (reverse).

Protein expression and purification

SEPT2/6/7 was expressed by cotransforming *Escherichia coli* BL21(DE3) cells with a bicistronic, kanamycin-resistant pET-28a(+) plasmid that expresses SEPT6 and His-SEPT7 in tandem, and an ampicillin-resistant pET-15b(+) plasmid that expresses untagged SEPT2 (Bai et al., 2013). His-SEPT9_1 was expressed by transforming *E. coli* BL21(DE3) cells with pET28a-SEPT9_i1 (Bai et al., 2013). Bacterial cultures of at least OD600 of 0.6 were induced with 0.5 mM IPTG for 16 h at 18°C, centrifuged at 5,000 rpm for 5 m at 4°C, and resuspended in buffer containing 1% Triton X-100, 50 mM Tris, pH 8.0, 150 mM NaCl, 10% glycerol, and 10 mM imidazole. Bacteria were lysed with a French pressure cell at 1,280 psi. Cell lysates were cleared using centrifugation (14,000 *g*) for 30 min at 4°C, and the supernatants were passed through Ni-NTA beads by gravity flow. The columns were washed with 10 ml washing buffer (50 mM Tris, pH 8.0, 300 mM NaCl, 10% glycerol, and 250 mM imidazole), and proteins were eluted with elution buffer (50 mM Tris, pH 8.0, 300 mM NaCl, 10% glycerol, and 250 mM imidazole). Purification of SEP2/6/7 was verified by size exclusion chromatography using an AKTA FPLC system (GE Healthcare). Purified proteins were dialyzed overnight in buffer containing 50 mM Tris, pH 8.0, 150 mM NaCl, and 10 mM imidazole.

Immunoprecipitations and immunoblots

For immunoprecipitations, an equal number of MDCK and SEPT2-YFP MDCK cells were lysed with buffer containing 50 mM Hepes, pH 7.4, 100 mM NaCl, 0.5% Triton X-100, 1 mM PMSF, and protease inhibitors (EMD Millipore) and incubated with anti-GFP antibody (3E6; Invitrogen) overnight at 4°C. Protein A beads (Thermo Fisher Scientific) were incubated for 4 h at 4°C and were stripped with SDS buffer at 95°C for 10 min. Equal volumes were resolved on a 10% SDS-PAGE gel and transferred to a nitrocellulose membrane using 100 V for 1 h at 4°C. Membranes were blocked with buffer containing 5% milk and 1% BSA for 1 h at 25°C. Rabbit antibodies against SEPT2 (1:5,000; Sigma-Aldrich), SEPT6 (1:5,000; Santa Cruz Biotechnology, Inc.), SEPT7 (1:8,000; IBL America), and SEPT9 (1:2,500; ITG Labs), and anti–rabbit or –mouse secondary antibodies (LiCor) conjugated to infrared dyes were diluted in buffer containing 2% BSA, 0.1% Tween-20, and 0.025% sodium azide, and sequentially incubated on each membrane before scanning with an imaging system (Odyssey; LI-COR).

To test for changes in SEPT9 expression after HGF treatment, MDCK cells were cultured on collagen-coated plates and stimulated with HGF for the indicated times. Cell lysates of equal protein concentration were run on a 10% SDS-PAGE gel, transferred to a nitrocellulose membrane, and probed using rabbit anti-SEPT9 (PTG Labs), mouse anti-actin (1:8,000; Sigma-Aldrich), and mouse anti-GAPDH (1:8,000; Abcam). The Western blot shown in Fig. 4 A is representative of three different experiments, which were reproduced with no limitations. To quantify SEPT9 overexpression in MDCK cells, untransfected cells and cells that stably overexpress SEPT9-mCherry were lysed, processed, and blotted (Fig. S2 D).

Immunofluorescence microscopy and quantifications

Cells were simultaneously fixed and extracted with 4% PFA in warm PBS buffer containing 0.1% Triton X-100 for 20 min, or fixed with 4% PFA in cytoskeleton buffer (10 mM MES, pH 6.1, 0.32 M sucrose, 138 mM KCl, 3 mM $MgCl_2$, and 2 mM EGTA) for 20 min and extracted with 0.5% Triton X-100 for 10 min (Fig. 3 D). Excess PFA was quenched with 0.25% ammonium chloride. Before antibody incubation, cells were blocked with PBS containing 2% BSA for 20 min. Rabbit antibodies against SEPT2 (N5N; a gift from M. Kinoshita, Nagoya University, Nagoya, Japan), SEPT6 (Tada et al., 2007), SEPT7 (IBL America), SEPT9 (ITG Labs), pY118-paxillin (EMD Millipore), myosin-IIA (Sigma-Aldrich), mouse antibodies to pSer19-MLC (Cell Signaling Technology) and paxillin (349; BD), and secondary donkey DyLight 488-, 594-, 647-conjugated F(ab′)2 to mouse or rabbit IgG (Jackson ImmunoResearch Laboratories, Inc.) were diluted in PBS with 2% BSA and 0.1% Triton X-100. F-actin was visualized using phalloidin conjugated to Alexa Fluor 488 or 647 (Life Technologies). Coverslips were mounted on slides using Vectashield (Vector Laboratories) or FluorSave (EMD) and imaged using a confocal laser-scanning microscope (FluoView 1000; Olympus) with a Plan-Apochromat 60×/1.42 NA objective lens. Optical sections (0.2 µm thick) were exported to Slidebook 5.0 (Intelligent Imaging Innovations), ImageJ, or Volocity (PerkinElmer) software for processing and quantification. Kymographs were generated in Slidebook by drawing a six-pixel-wide line down the center of a growing FA marked by paxillin or ABP140-ABD. Super-resolution SIM was performed using the DeltaVision OMX V4 (GE Healthcare) microscope with a 60×/1.42 NA objective and immersion oil lenses with a refractive index of 1.514. A z-step size of 0.125 µm was used and images were acquired with sCMOS pco.edge cameras (PCO) and reconstructed with softWoRx software (Applied Precision).

FA sizes were quantified using masks of paxillin fluorescence intensity segmentation; the area of individual masks was exported to Excel and quantified. FA distance from the cell edge was measured by converting the phalloidin-stained cell into a binary image, which was subsequently inverted and transformed into a Euclidean distance map (Schober et al., 2007). FAs were overlaid on the map, and the distance from the FA center to the cell edge was measured. To assess relative levels of pTyr118 paxillin to total paxillin, confocal images were obtained using identical laser settings between control and septin-depleted samples. Individual FAs were masked using intensity segmentation and the ratios were derived from the sum intensities.

Colocalization of septins with actin in the leading cell edge was quantified in background-subtracted images using the Mander's coefficient analysis in Slidebook. Fluorescence intensity of actin as a function of the

distance from the cell edge was quantified from confocal images, which were acquired during one sitting at identical laser intensities. Protrusions at the leading cell edge were sampled 2–3 times using a 10 µm × 1 µm line scan drawn perpendicular from the cortex and were averaged and plotted using custom software (supplemental code 1) written in MATLAB (MathWorks). The number of RSFs per micrometer was calculated by drawing a line parallel to the cell edge and counting the number of radial fibers that intersected with the line. Fluorescence intensity ratios of pSer19-myosin II light chain to myosin IIA heavy chain (Fig. S3) were quantified by masking 5-µm segments of the TAs parallel to the leading cell edge. In each cell, the sum intensities of at least six different segments were analyzed.

To visualize 3D cyst structure (Fig. 4 C), gels were briefly treated with collagenase (Sigma-Aldrich) in PBS at 37°C and fixed with 4% PFA in PBS with 0.5% Triton X-100. Gels were incubated with phalloidin for 1 h under gentle agitation and mounted in Vectashield. Optical sections (1.25 µm thick) were stacked as mass projections. The number of extensions per cyst and the number of cells per extension were quantified and plotted. Extensions were defined as protrusions from the main cyst body consisting of three cells or more. To quantify single cell morphology in 3D (Fig. 4 I), gels were fixed, stained, and mounted using the same method but without the initial collagenase treatment. The long and short axes were measured in Slidebook to derive the axial ratio of each cell. To measure the velocity of cell movement in a 3D matrix (Fig. 4 H), time-lapse optical sections were imported into the Volocity software, which identified, tracked, and quantified the movement of the cell centroid.

Time-lapse imaging

All live imaging experiments were performed at 37°C in DME lacking Phenol red supplemented with 0.5% FBS, 1% PSK, and 20 mM Hepes. Widefield microscopy was performed with an inverted microscope (IX-81; Olympus) equipped with a motorized stage (ProScanII; Prior), a camera (OrcaR2; Hamamatsu Photonics), a custom-built stage-top chamber and temperature controller (Air-Therm ATX; World Precision Instruments), and the Slidebook 5.0 software. Fluorescent images were captured every 20 s with a Plan-Apochromat 60×/1.40 NA objective lens (Olympus). Spinning disk confocal microscopy was performed at 37°C using an inverted microscope (IX-71; Olympus) equipped with a camera (ImagEM; Hamamatsu Photonics), an airstream incubator (LiveCell; Pathology Devices), scan head (CSU10; Yokogawa Electric Corporation), and the MetaMorph software (Molecular Devices). Fluorescent images were captured every 20 s with a 60× 1.49 NA objective lens. Total internal reflection fluorescence (TIRF) microscopy was performed at 37°C with the DeltaVision OMX V4 inverted microscope (GE Healthcare) equipped with 60×/1.49 NA TIRF objective lens (Olympus), motorized stage, sCMOS pco.edge cameras (PCO), stage-top incubator with temperature controller, and the softWoRx software. 3D cell migration experiments were performed using a laser scanning confocal microscope (LSM700; Carl Zeiss) equipped with a stage-top incubator and temperature controller (XL modules; Carl Zeiss), and the Zen software (Carl Zeiss). 1-µm optical sections were acquired every 2 min with a 40× C-Apochromat/1.2 NA water objective lens (Carl Zeiss). Videos were rendered using the Photoshop software (Adobe).

Quantification of FA dynamics

FA dynamics were obtained using the stable MDCK-paxillin-GFP cell line and TIRF microscopy; background subtraction and photobleach correction algorithms in the Slidebook software were applied to normalize fluorescence intensities. Individual FA lifetimes were quantified from the length of each adhesion signal in three cells using the open-source Focal Adhesion Analysis Server (Berginski and Gomez, 2013). FA assembly and disassembly rates were quantified as described previously (Webb et al., 2004). In brief, individual FAs were masked in Slidebook and a semilogrithmic plot of paxillin intensity as a function of time was generated. The rate constants were derived from the slopes of 45 adhesions from the leading edge (three cells per condition).

Low-speed cosedimentation assay

Human platelet actin (Cytoskeleton, Inc.) in G buffer (5 mM Tris-HCl and 0.2 mM $CaCl_2$) was polymerized using F buffer (20 mM Hepes, 100 mM KCl, and 1 mM $MgCl_2$) supplemented with 0.5 mM ATP and 4 mM DTT for 1 h at 25°C to generate F-actin. 2 µM recombinant SEPT2/6/7 and 4 µM recombinant his-tagged SEPT9 were incubated with 2 µM F-actin for 1 h at 25°C and centrifuged atop a glycerol cushion (20 mM Hepes, 100 mM NaCl, 1 mM $MgCl_2$, and 10% glycerol) at 8,000 *g* for 20 min at 25°C. Equal volumes of the supernatant and pellet fractions were resolved using a 7.5% SDS-PAGE gel and stained with Coomassie brilliant blue.

Electron microscopy

Skeletal striated muscle G-actin (2.5 µM) was polymerized in 10 mM Hepes buffer, pH 7.4, 100 mM KCl, 1 mM $MgCl_2$, 0.5 mM DTT, and 0.5 mM ATP for 2 h. Actin filaments were incubated with 14 µM His-SEPT6 or His-SEPT9 for 15–30 min at 4°C. To visualize complexes of F-actin with septins, aliquots (10 µl) were applied to glow-discharged carbon-coated grids (Electron Microscopy Sciences) and stained with 2% uranyl acetate. The grids were examined in a transmission electron microscope (TEM; 1200EXII; JEOL Inc.) under regular dose conditions at an accelerating voltage of 70 keV. The images shown in Fig. 3 (F and G) are representative of similar results obtained from three independent experiments.

Transmigration assays

786-O cells were transfected with plasmids encoding for the indicated constructs for 48 h, trypsinized, and plated on collagen-coated transwell filters (8 µm pore) for 12 h. Filters were fixed with 4% PFA in PBS and stained for nuclei with DAPI. Apical and basolateral sections were imaged at 20× magnification using confocal microscopy. The number of transfected cells in each section was quantified and plotted in Excel.

Statistical analyses

Datasets were analyzed using R and the Excel software. Normal distribution and equal variance were assessed using the Shapiro and Levene tests, respectively. Datasets with normal distribution and variance were analyzed using an unpaired student's *t* test. Datasets that did not exhibit normal distributions or variance were further analyzed using the Kruskal-Wallis nonparametric ANOVA. All values represent the mean ± SEM.

Online supplemental material

Fig. S1 shows colocalization of septins 2, 6, 7, and 9 at the leading edge of HGF-treated MDCK cells. Fig. S2 shows septin expression in SEPT2- and SEPT9-depleted and SEPT9-mCherry–overexpressing cells. Fig. S3 shows that phosphorylated myosin RLC (pSer19-MLC) is not affected by septin depletion, whereas FAs are rescued by the myosin IIA N93K heavy chain in septin-depleted cells. Video 1 shows a 3D view of septin localization at the interface of TA and RSFs rotated round the xy plane. Video 2 shows TIRF microscopy of paxillin-GFP dynamics at the leading cell edge of control and septin-depleted cells. Video 3 shows TIRF microscopy of ABP140-ABD-mCherry at the leading cell edge in control and septin-depleted cells. Video 4 shows the motility of dissociated single MDCK cells in a 3D matrix after treatment with control and SEPT9 shRNAs. Code 1 is a custom MATLAB code that generates an intensity matrix from the microscope image and averages the intensity of each column. Online supplemental material is available at http://www.jcb.org/cgi/content/full/jcb.201405050/DC1.

We thank Drs. James Nelson (Stanford University), Rick Horwitz (University of Virginia), Cristina Montagna (Albert Einstein College of Medicine), and Pere Roca-Cusachs (University of Barcelona) for constructs and cell lines. We are thankful to Andrea Stout (University of Pennsylvania) for help with spinning disk confocal microscopy, which was performed at the CDB Microscopy Core. All other microscopy was conducted at the Cell Imaging Center (Drexel University).

The work was supported by National Institutes of Health grants CA176910 to L. Dolat and GM097664 to E.T. Spiliotis.

The authors declare no competing financial interests.

Submitted: 13 May 2014
Accepted: 18 September 2014

References

Bai, X., J.R. Bowen, T.K. Knox, K. Zhou, M. Pendziwiat, G. Kuhlenbäumer, C.V. Sindelar, and E.T. Spiliotis. 2013. Novel septin 9 repeat motifs altered in neuralgic amyotrophy bind and bundle microtubules. *J. Cell Biol.* 203:895–905. http://dx.doi.org/10.1083/jcb.201308068

Berginski, M.E., and S.M. Gomez. 2013. The Focal Adhesion Analysis Server: a web tool for analyzing focal adhesion dynamics. *F1000 Res.* 2:68.

Bowen, J.R., D. Hwang, X. Bai, D. Roy, and E.T. Spiliotis. 2011. Septin GTPases spatially guide microtubule organization and plus end dynamics in polarizing epithelia. *J. Cell Biol.* 194:187–197. http://dx.doi.org/10.1083/jcb.201102076

Bravo-Cordero, J.J., L. Hodgson, and J. Condeelis. 2012. Directed cell invasion and migration during metastasis. *Curr. Opin. Cell Biol.* 24:277–283. http://dx.doi.org/10.1016/j.ceb.2011.12.004

Burridge, K., and E.S. Wittchen. 2013. The tension mounts: stress fibers as force-generating mechanotransducers. *J. Cell Biol.* 200:9–19. http://dx.doi.org/10.1083/jcb.201210090

Chacko, A.D., P.L. Hyland, S.S. McDade, P.W. Hamilton, S.H. Russell, and P.A. Hall. 2005. SEPT9_v4 expression induces morphological change, increased motility and disturbed polarity. *J. Pathol.* 206:458–465. http://dx.doi.org/10.1002/path.1794

Choi, C.K., M. Vicente-Manzanares, J. Zareno, L.A. Whitmore, A. Mogilner, and A.R. Horwitz. 2008. Actin and α-actinin orchestrate the assembly and maturation of nascent adhesions in a myosin II motor-independent manner. *Nat. Cell Biol.* 10:1039–1050. http://dx.doi.org/10.1038/ncb1763

Connolly, D., I. Abdesselam, P. Verdier-Pinard, and C. Montagna. 2011a. Septin roles in tumorigenesis. *Biol. Chem.* 392:725–738. http://dx.doi.org/10.1515/BC.2011.073

Connolly, D., Z. Yang, M. Castaldi, N. Simmons, M.H. Oktay, S. Coniglio, M.J. Fazzari, P. Verdier-Pinard, and C. Montagna. 2011b. Septin 9 isoform expression, localization and epigenetic changes during human and mouse breast cancer progression. *Breast Cancer Res.* 13:R76. http://dx.doi.org/10.1186/bcr2924

Craven, R.A., S. Hanrahan, N. Totty, P. Harnden, A.J. Stanley, E.R. Maher, A.L. Harris, W.S. Trimble, P.J. Selby, and R.E. Banks. 2006. Proteomic identification of a role for the von Hippel Lindau tumour suppressor in changes in the expression of mitochondrial proteins and septin 2 in renal cell carcinoma. *Proteomics*. 6:3880–3893. http://dx.doi.org/10.1002/pmic.200500811

De Craene, B., and G. Berx. 2013. Regulatory networks defining EMT during cancer initiation and progression. *Nat. Rev. Cancer*. 13:97–110. http://dx.doi.org/10.1038/nrc3447

Debnath, J., and J.S. Brugge. 2005. Modelling glandular epithelial cancers in three-dimensional cultures. *Nat. Rev. Cancer*. 5:675–688. http://dx.doi.org/10.1038/nrc1695

de Rooij, J., A. Kerstens, G. Danuser, M.A. Schwartz, and C.M. Waterman-Storer. 2005. Integrin-dependent actomyosin contraction regulates epithelial cell scattering. *J. Cell Biol.* 171:153–164. http://dx.doi.org/10.1083/jcb.200506152

Dolat, L., Q. Hu, and E.T. Spiliotis. 2014. Septin functions in organ system physiology and pathology. *Biol. Chem.* 395:123–141. http://dx.doi.org/10.1515/hsz-2013-0233

Dressler, G. 2002. Tubulogenesis in the developing mammalian kidney. *Trends Cell Biol.* 12:390–395. http://dx.doi.org/10.1016/S0962-8924(02)02334-6

Friedl, P., and K. Wolf. 2010. Plasticity of cell migration: a multiscale tuning model. *J. Cell Biol.* 188:11–19. http://dx.doi.org/10.1083/jcb.200909003

Gardel, M.L., I.C. Schneider, Y. Aratyn-Schaus, and C.M. Waterman. 2010. Mechanical integration of actin and adhesion dynamics in cell migration. *Annu. Rev. Cell Dev. Biol.* 26:315–333. http://dx.doi.org/10.1146/annurev.cellbio.011209.122036

Geiger, B., and K.M. Yamada. 2011. Molecular architecture and function of matrix adhesions. *Cold Spring Harb. Perspect. Biol.* 3:a005033. http://dx.doi.org/10.1101/cshperspect.a005033

Guarino, M., B. Rubino, and G. Ballabio. 2007. The role of epithelial-mesenchymal transition in cancer pathology. *Pathology*. 39:305–318. http://dx.doi.org/10.1080/00313020701329914

Hu, Q., W.J. Nelson, and E.T. Spiliotis. 2008. Forchlorfenuron alters mammalian septin assembly, organization, and dynamics. *J. Biol. Chem.* 283:29563–29571. http://dx.doi.org/10.1074/jbc.M804962200

Joo, E., M.C. Surka, and W.S. Trimble. 2007. Mammalian SEPT2 is required for scaffolding nonmuscle myosin II and its kinases. *Dev. Cell*. 13:677–690. http://dx.doi.org/10.1016/j.devcel.2007.09.001

Kim, M.S., C.D. Froese, M.P. Estey, and W.S. Trimble. 2011. SEPT9 occupies the terminal positions in septin octamers and mediates polymerization-dependent functions in abscission. *J. Cell Biol.* 195:815–826. http://dx.doi.org/10.1083/jcb.201106131

Kinoshita, M., S. Kumar, A. Mizoguchi, C. Ide, A. Kinoshita, T. Haraguchi, Y. Hiraoka, and M. Noda. 1997. Nedd5, a mammalian septin, is a novel cytoskeletal component interacting with actin-based structures. *Genes Dev.* 11:1535–1547. http://dx.doi.org/10.1101/gad.11.12.1535

Kinoshita, M., C.M. Field, M.L. Coughlin, A.F. Straight, and T.J. Mitchison. 2002. Self- and actin-templated assembly of Mammalian septins. *Dev. Cell*. 3:791–802. http://dx.doi.org/10.1016/S1534-5807(02)00366-0

Kremer, B.E., L.A. Adang, and I.G. Macara. 2007. Septins regulate actin organization and cell-cycle arrest through nuclear accumulation of NCK mediated by SOCS7. *Cell*. 130:837–850. http://dx.doi.org/10.1016/j.cell.2007.06.053

Leipe, D.D., Y.I. Wolf, E.V. Koonin, and L. Aravind. 2002. Classification and evolution of P-loop GTPases and related ATPases. *J. Mol. Biol.* 317:41–72. http://dx.doi.org/10.1006/jmbi.2001.5378

Lim, J., and J.P. Thiery. 2012. Epithelial-mesenchymal transitions: insights from development. *Development*. 139:3471–3486. http://dx.doi.org/10.1242/dev.071209

Liu, Y. 2010. New insights into epithelial-mesenchymal transition in kidney fibrosis. *J. Am. Soc. Nephrol.* 21:212–222. http://dx.doi.org/10.1681/ASN.2008121226

Mavrakis, M., Y. Azou-Gros, F.-C. Tsai, J. Alvarado, A. Bertin, F. Iv, A. Kress, S. Brasselet, G.H. Koenderink, and T. Lecuit. 2014. Septins promote F-actin ring formation by crosslinking actin filaments into curved bundles. *Nat. Cell Biol.* 16:322–334. http://dx.doi.org/10.1038/ncb2921

Mostowy, S., and P. Cossart. 2012. Septins: the fourth component of the cytoskeleton. *Nat. Rev. Mol. Cell Biol.* 13:183–194.

Oakes, P.W., Y. Beckham, J. Stricker, and M.L. Gardel. 2012. Tension is required but not sufficient for focal adhesion maturation without a stress fiber template. *J. Cell Biol.* 196:363–374. http://dx.doi.org/10.1083/jcb.201107042

Parri, M., and P. Chiarugi. 2010. Rac and Rho GTPases in cancer cell motility control. *Cell Commun. Signal.* 8:23. http://dx.doi.org/10.1186/1478-811X-8-23

Parsons, J.T., A.R. Horwitz, and M.A. Schwartz. 2010. Cell adhesion: integrating cytoskeletal dynamics and cellular tension. *Nat. Rev. Mol. Cell Biol.* 11:633–643. http://dx.doi.org/10.1038/nrm2957

Raftopoulou, M., and A. Hall. 2004. Cell migration: Rho GTPases lead the way. *Dev. Biol.* 265:23–32. http://dx.doi.org/10.1016/j.ydbio.2003.06.003

Roca-Cusachs, P., A. del Rio, E. Puklin-Faucher, N.C. Gauthier, N. Biais, and M.P. Sheetz. 2013. Integrin-dependent force transmission to the extracellular matrix by α-actinin triggers adhesion maturation. *Proc. Natl. Acad. Sci. USA*. 110:E1361–E1370. http://dx.doi.org/10.1073/pnas.1220723110

Schmidt, K., and B.J. Nichols. 2004. Functional interdependence between septin and actin cytoskeleton. *BMC Cell Biol.* 5:43. http://dx.doi.org/10.1186/1471-2121-5-43

Schober, M., S. Raghavan, M. Nikolova, L. Polak, H.A. Pasolli, H.E. Beggs, L.F. Reichardt, and E. Fuchs. 2007. Focal adhesion kinase modulates tension signaling to control actin and focal adhesion dynamics. *J. Cell Biol.* 176:667–680. http://dx.doi.org/10.1083/jcb.200608010

Schwartz, M.A. 2010. Integrins and extracellular matrix in mechanotransduction. *Cold Spring Harb. Perspect. Biol.* 2:a005066. http://dx.doi.org/10.1101/cshperspect.a005066

Sellin, M.E., L. Sandblad, S. Stenmark, and M. Gullberg. 2011. Deciphering the rules governing assembly order of mammalian septin complexes. *Mol. Biol. Cell*. 22:3152–3164. http://dx.doi.org/10.1091/mbc.E11-03-0253

Shinoda, T., H. Ito, K. Sudo, I. Iwamoto, R. Morishita, and K. Nagata. 2010. Septin 14 is involved in cortical neuronal migration via interaction with Septin 4. *Mol. Biol. Cell*. 21:1324–1334. http://dx.doi.org/10.1091/mbc.E09-10-0869

Spiliotis, E.T., M. Kinoshita, and W.J. Nelson. 2005. A mitotic septin scaffold required for mammalian chromosome congression and segregation. *Science*. 307:1781–1785. http://dx.doi.org/10.1126/science.1106823

Stricker, J., Y. Beckham, M.W. Davidson, and M.L. Gardel. 2013. Myosin II-mediated focal adhesion maturation is tension insensitive. *PLoS ONE*. 8:e70652. http://dx.doi.org/10.1371/journal.pone.0070652

Tada, T., A. Simonetta, M. Batterton, M. Kinoshita, D. Edbauer, and M. Sheng. 2007. Role of Septin cytoskeleton in spine morphogenesis and dendrite development in neurons. *Curr. Biol.* 17:1752–1758. http://dx.doi.org/10.1016/j.cub.2007.09.039

Thiery, J.P., H. Acloque, R.Y. Huang, and M.A. Nieto. 2009. Epithelial-mesenchymal transitions in development and disease. *Cell*. 139:871–890. http://dx.doi.org/10.1016/j.cell.2009.11.007

Tooley, A.J., J. Gilden, J. Jacobelli, P. Beemiller, W.S. Trimble, M. Kinoshita, and M.F. Krummel. 2009. Amoeboid T lymphocytes require the septin cytoskeleton for cortical integrity and persistent motility. *Nat. Cell Biol.* 11:17–26. http://dx.doi.org/10.1038/ncb1808

Vicente-Manzanares, M., X. Ma, R.S. Adelstein, and A.R. Horwitz. 2009. Non-muscle myosin II takes centre stage in cell adhesion and migration. *Nat. Rev. Mol. Cell Biol.* 10:778–790. http://dx.doi.org/10.1038/nrm2786

Webb, D.J., K. Donais, L.A. Whitmore, S.M. Thomas, C.E. Turner, J.T. Parsons, and A.F. Horwitz. 2004. FAK-Src signalling through paxillin, ERK and MLCK regulates adhesion disassembly. *Nat. Cell Biol.* 6:154–161. http://dx.doi.org/10.1038/ncb1094

Weirich, C.S., J.P. Erzberger, and Y. Barral. 2008. The septin family of GTPases: architecture and dynamics. *Nat. Rev. Mol. Cell Biol.* 9:478–489. http://dx.doi.org/10.1038/nrm2407

West, K.A., H. Zhang, M.C. Brown, S.N. Nikolopoulos, M.C. Riedy, A.F. Horwitz, and C.E. Turner. 2001. The LD4 motif of paxillin regulates cell spreading and motility through an interaction with paxillin kinase linker (PKL). *J. Cell Biol.* 154:161–176. http://dx.doi.org/10.1083/jcb.200101039

Yamada, S., and W.J. Nelson. 2007. Localized zones of Rho and Rac activities drive initiation and expansion of epithelial cell-cell adhesion. *J. Cell Biol.* 178:517–527. http://dx.doi.org/10.1083/jcb.200701058

Zaidel-Bar, R., R. Milo, Z. Kam, and B. Geiger. 2007. A paxillin tyrosine phosphorylation switch regulates the assembly and form of cell-matrix adhesions. *J. Cell Sci.* 120:137–148. http://dx.doi.org/10.1242/jcs.03314

Zegers, M.M., L.E. O'Brien, W. Yu, A. Datta, and K.E. Mostov. 2003. Epithelial polarity and tubulogenesis in vitro. *Trends Cell Biol.* 13:169–176. http://dx.doi.org/10.1016/S0962-8924(03)00036-9